Coherence locking in a parallel NMR probe defends against gradient field spillover

Mengjia He[1], Neil MacKinnon[1*], Dominique Buyens[1], Burkhard Luy[2,3] and Jan G. Korvink[1*]

[1]*Institute of Microstructure Technology, Karlsruhe Institute of Technology, Eggenstein-Leopoldshafen, Germany.*

[2]*Institute for Biological Interfaces 4 - Magnetic Resonance, Karlsruhe Institute of Technology, Eggenstein-Leopoldshafen, Germany.*

[3]*Institute of Organic Chemistry, Karlsruhe Institute of Technology, Karlsruhe, Germany.*

[*] Corresponding authors: neil.mackinnon@kit.edu, jan.korvink@kit.edu

Abstract

The implementation of parallel nuclear magnetic resonance detection aims to enhance measurement throughput in support of high throughput screening applications including, for example, drug discovery. In support of modern pulse sequences and solvent suppression methods, each detection site must have independent pulsed field gradient capabilities. Hereby, a challenge is introduced, in which the local gradients applied in parallel detectors introduce field spillover in adjacent channels, leading to spin dephasing and hence to signal suppression. This study proposes a compensation scheme employing optimized pulses to achieve coherence locking during gradient pulse periods. The design of coherence-locking pulses utilizes optimal control to address gradient-induced field inhomogeneity. These pulses are applied in a PGSE experiment, and a parallel HSQC experiment, demonstrating their effectiveness in protecting the desired coherences from gradient field spillover. This compensation scheme presents a valuable solution for magnetic resonance probes equipped with parallel and independently switchable gradient coils.

1 Introduction

While nuclear magnetic resonance (NMR) technology is routinely employed to analyze large sets of chemical samples and monitor dynamic biochemical processes, achieving a high-throughput capability has remained a challenge. Simultaneous detection of multiple samples enhances throughput (MacNamara et al., 1999; Kupče et al., 2021), while composite detection using a bundle of isolated capillaries achieves high throughput with simpler hardware (Ross et al.,

25   2001). Greater parallel independence relies on multiple radiofrequency (RF) coils for parallel excitation and reception, along with pulsed gradient fields (MacNamara et al., 1999; Hou et al., 1999) or alternative detection (Li et al., 1999) to separate the parallel detectors. Parallel NMR has been combined with classical pulse sequences (Wang et al., 2004), reaction kinetic measurements (Ciobanu et al., 2003), and dissolution dynamic nuclear polarization (Kim et al., 2016). Integrating multiple coils into a single silicon chip has demonstrated portable NMR applications (Lei et al., 2020),

30   employing time-interleaved pulses for RF decoupling. For full parallel and independent operation, each detector typically integrates individual RF coils, gradient coils, and shimming units (Cheng et al., 2022; Becker et al., 2023). However, practical limitations in electromagnetic shielding design, particularly in dense and highly composite arrays, result in field leakage and inter-channel coupling. RF decoupling schemes have been reported recently regarding both the excitation and reception stages (He et al., 2024). The pulsed gradient field spillover among parallel detectors directly induces B_0

35   inhomogeneity, leading to spin dephasing, thus posing a challenge that remains to be addressed.

A straightforward approach to mitigate spin dephasing to B_0 inhomogeneity is by transferring the spin state to longitudinal magnetization, e.g., I_z for single spins or $I_z S_z$ for coupled spins. However, this proves challenging when the initial state is unknown or time constraints exist. Spin locking via RF pulses is an effective strategy for preserving spin magnetization, i.e., a long hard pulse with a defined phase is applied to protect a specific coherence, such as I_x

40   or I_y. In heteronuclear experiments, continuous wave spin-locking fields have been utilized to render proton multiple quantum coherence immune to ^{1}H-^{1}H J coupling (Grzesiek and Bax, 1995). Spin locking induced crossing has a wide range of applications, including preparation of singlet states (DeVience et al., 2013a, b; Rodin et al., 2018), excitation of long-lived states (Sonnefeld et al., 2022; Barskiy et al., 2017; DeVience et al., 2015), and low field spectroscopy (DeVience et al., 2021; Kovtunov et al., 2014). Moreover, traditional spin-locking pulses have been adapted to address B_0 and B_1

45   inhomogeneity in quantifying the rotating frame relaxation time (Jiang and Chen, 2018; Gram et al., 2021).

In this study, we used optimal control to design cyclic pulses that preserve the desired coherence, such as I^- for a single spin and $I^- S^+$ for a coupled spin pair. The coherence-locking by optimal control (CLOC) pulses exhibit robustness against a range of B_0 drifts, effectively mitigating gradient spillover effects in parallel NMR experiments. Multiple CLOC blocks are inserted to safeguard specific coherence transfer pathways when the pulse sequence incorporates a series of gradient

50   pulses. Using this protection idea, we demonstrated that the parallel HSQC experiment retains its SNR through coherence locking.

2 Results and Discussion

Fig. 1a shows the geometry of the parallel detector used in the experiments. Each detector is equipped with a Helmholtz gradient coil and a stripline RF coil. To provide an initial view, three scenarios were considered for the HSQC experiments. The first scenario, serving as a reference, is shown in the black part of Fig. 1b. A standard HSQC pulse sequence was used, in which gradient pulses with a ratio of $2 : 2 : -1$ were applied to select the $S^+ \rightarrow S^+ \rightarrow I^+ \rightarrow I^-$ coherence transfer pathway. The second scenario, depicted in orange in Fig. 1b, introduces an additional set of gradient pulses, G_C. These gradients, independent of G, were applied with a ratio of $2 : 2 : 1$ and were temporally shifted relative to the primary gradients to induce gradient field spillover. The third scenario, indicated in blue in Fig. 1b, integrates three CLOC blocks along with G_C into the HSQC sequence. The first and second CLOC blocks were applied to ^{13}C, while the third was applied to ^1H.
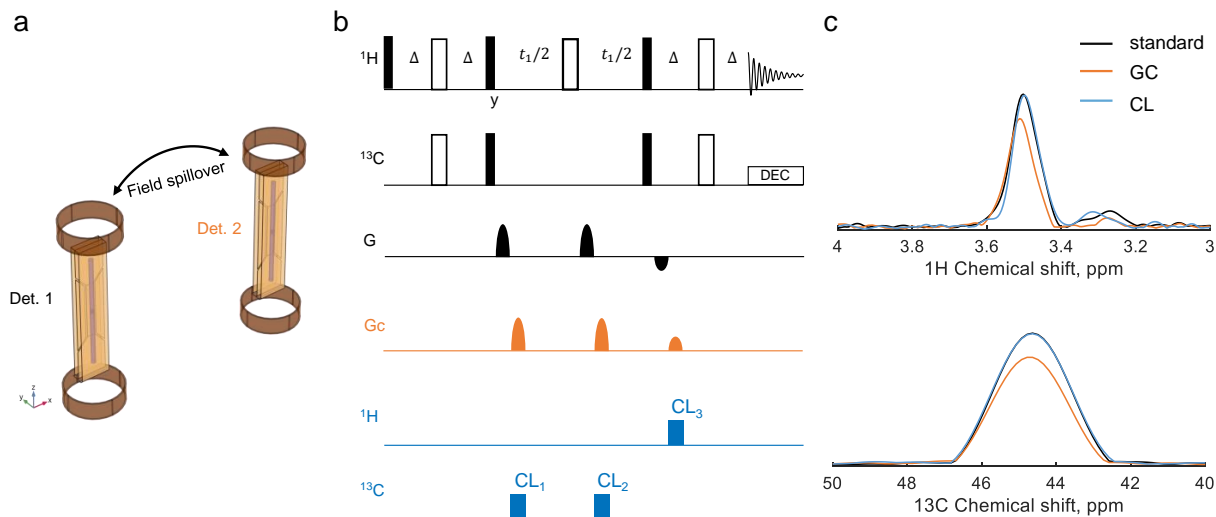
Figure 1. Setup of the HSQC experiment under gradient filed spillover. (a) The parallel detector geometry, where each detector is equipped with a Helmholtz gradient coil and a stripline. (b) Pulse sequences of the three experimental HSQC scenarios. The black part represents a standard HSQC pulse sequence, with a gradient pulse ratio of $2 : 2 : -1$ to select the $S^+ \rightarrow S^+ \rightarrow I^+ \rightarrow I^-$ coherence pathway, defining the first scenario. The orange part (G_c) represents additional gradient pulses from a second detector, set at a $2 : 2 : 1$ ratio, inserted into HSQC as coupled gradients, defining the second scenario. The blue section indicates the insertion of CLOC pulses into HSQC, aligned with the coupled gradient pulses, representing the third scenario. Specifically, CL_1 and CL_2 are applied to ^{13}C, while CL_3 is applied to ^{1}H. (c) The 1D projections of HSQC spectra corresponding to the three experimental scenarios, obtained using 0.6 M glycine-2-^{13}C in D_2O.

Experiments were conducted for all three scenarios using glycine-2-^{13}C as the test sample, and the resulting spectra are shown in Fig. 1c. Compared to the reference spectrum from the standard HSQC experiment, the gradient coupling scenario resulted in a 20% signal loss. In HSQC, a coherence pathway is refocused only if the net effect of all gradient pulses is zero. Additional gradients can disrupt this balance, causing dephasing and signal loss, which can happen when separate gradient-enhanced experiments are run in parallel at two detector sites. However, including CLOC blocks resulted in a signal intensity equal to the reference, indicating that the relevant coherences were preserved. Different gradient ratios are utilized in a parallel probe if multiple detectors execute different experiments or employ the same sequence but select distinct coherence pathways. The gradient spillover disrupts the intended coherence, and coherence locking can mitigate the dephasing effect in these scenarios. Note that if two detectors use identical sequences with the same gradient pulse

ratio, the total gradient ratio remains unchanged. Consequently, no gradient defense mechanisms are required, as shown in Fig. S2b.

Following the overview, we detail the gradient coupling issue and the coherence-locking compensation solution. The simulation results quantifying the gradient spillover effect are presented in Fig. S1, and the measurement of the gradient spillover ratio is provided below. Firstly, the maximum gradient strength of the parallel probe was measured using the pulsed gradient spin echo (PGSE) experiment, for a sample of 10% H_2O/90% D_2O with a diffusion constant (Holz and Weingartner, 1991) $D = 1.9 \times 10^{-9}$ $m^2 \cdot s^{-1}$. The ratio of the signal to the maximum value is a function of the applied gradient amplitude (Stejskal and Tanner, 1965),

$$\ln(I_g/I_0) = -[\gamma^2 \delta^2 G^2 (\Delta - \delta)]D \tag{1}$$

where $\delta = 1$ ms is the gradient pulse length, $\Delta = 7$ ms is the interval between two gradient pulses, and $\gamma = 2.675 \times 10^8$ $rad \cdot s^{-1} \cdot T^{-1}$ is the proton gyromagnetic ratio. Curve fitting yielded a maximum gradient of $G_{max} = 103.06$ G/cm, see Fig. 2a.
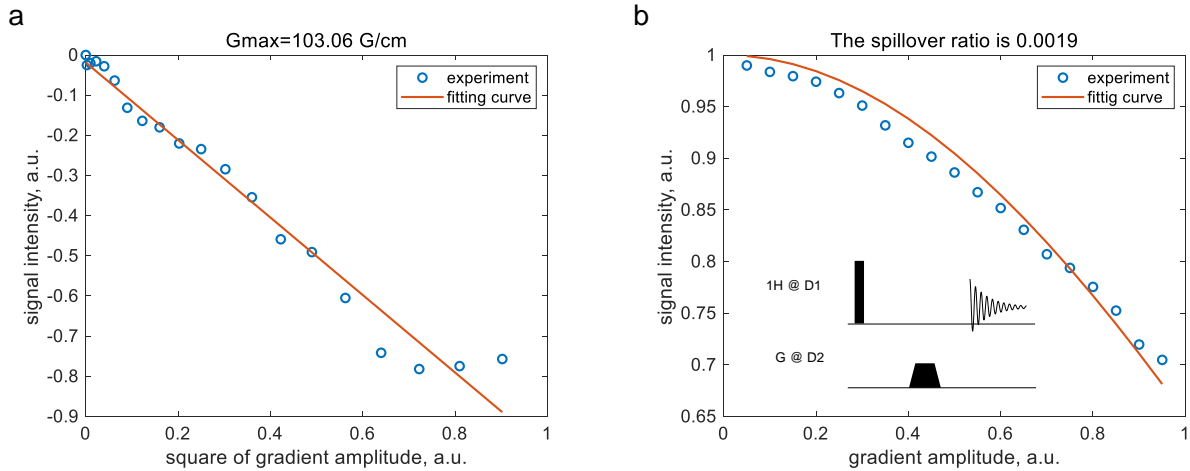
Figure 2. Measurement of the gradient spillover ratio for the parallel detector in Fig. 1, using 10% H_2O/90% D_2O. (a) Signal intensity as a function of gradient amplitude in the PGSE sequence, the maximum gradient amplitude was calculated to be $G_{max} = 103.06$ G/cm at a 100% gradient. (b) Signal intensity as a function of coupling gradient amplitude in a pulse-acquisition experiment, the gradient spillover ratio was calculated to be $R_G = 1.9 \times 10^{-3}$. The circles and the solid lines represent the experimental data and the fitted curves, respectively.

The gradient spillover ratio was then measured in a pulse-acquisition experiment, while a gradient pulse was applied to the second detector, see the insert of Fig. 2b. The ratio of the signal to the maximum value is a function of the applied gradient amplitude,

$$\frac{I_g}{I_0} = \frac{\sin(kg)}{kg} \tag{2}$$

where $k = l/2 \cdot \gamma \cdot R_G \cdot G_{\max} \cdot \int g(t)\, dt$, $l = 6.5$ mm is the detection zone length, and $\int g(t)\, dt = 0.9$ ms is the time integral of the trapezoidal gradient pulse. The gradient spillover ratio was determined by curve fitting as $R_G = 1.9 \times 10^{-3}$.

Depending on the gradient pulses used, the impact of such a gradient spillover can differ. For example, the gradient coupling resulted in 20% signal loss in an HSQC experiment, as shown in Fig. 1c. Strong gradients are essential for diffusion experiments, as they can induce a coupled gradient of $0.20\,\mathrm{G/cm}$ in the neighboring detector, making gradient coupling a critical concern. Here, we propose a compensation scheme utilizing RF pulses to mitigate the gradient spillover. The idea is to protect desired coherences from unwanted field gradients using CLOC pulses, which are time-aligned with the coupling gradient pulses. For example, a gradient pulse applied to detector 1 can be compensated by simultaneously applying a CLOC pulse to detector 2. This scheme was demonstrated with a PGSE experiment and a parallel HSQC experiment.
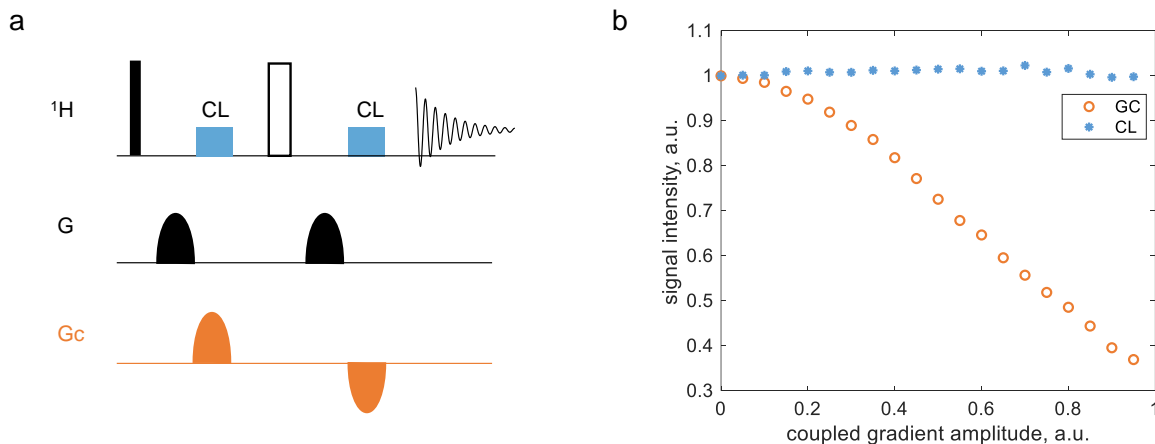
Figure 3. Coherence-locking test in PGSE using $0.6\,\mathrm{M}$ glycine-2-^{13}C in D_2O. (a) The pulse sequence, where the ^{1}H pulse and G were applied to detector 1, and the G_c was applied to detector 2. (b) The signal intensity of the water peak, normalized to its value when $G_c = 0$, was plotted as a function of G_c, with G fixed at 10%.

As shown in Fig. 3a, an additional gradient, G_C, was introduced as the coupling component in a standard PGSE sequence, temporally shifted relative to the primary gradient. When G_C disrupted the strength balance on either side of the inversion pulse, two CLOC pulses were applied, aligned with each block of G_C, to counteract gradient spillover. These CLOC pulses preserved spin coherence, protecting I^+ during the first G_C period and I^- during the second. Alternatively, the pulses can enable effective cyclic propagation (i.e., $\mathbf{U} = \mathbf{1}$), which is a stricter condition and was selected as our design target. Details of pulse optimization are provided later. The proposed coherence locking in PGSE was tested using $0.6\,\mathrm{M}$ glycine-2-^{13}C in D_2O, with results shown in Fig. 3b. The G_C amplitude was swept from 0 to 95% in the pulse program while the G was fixed at 10%, and the water peak intensity was extracted and normalized to its value at $G_C = 0$ for comparison. Compared to the large signal loss in the gradient coupling case, the CLOC pulse effectively restored the signal intensity.
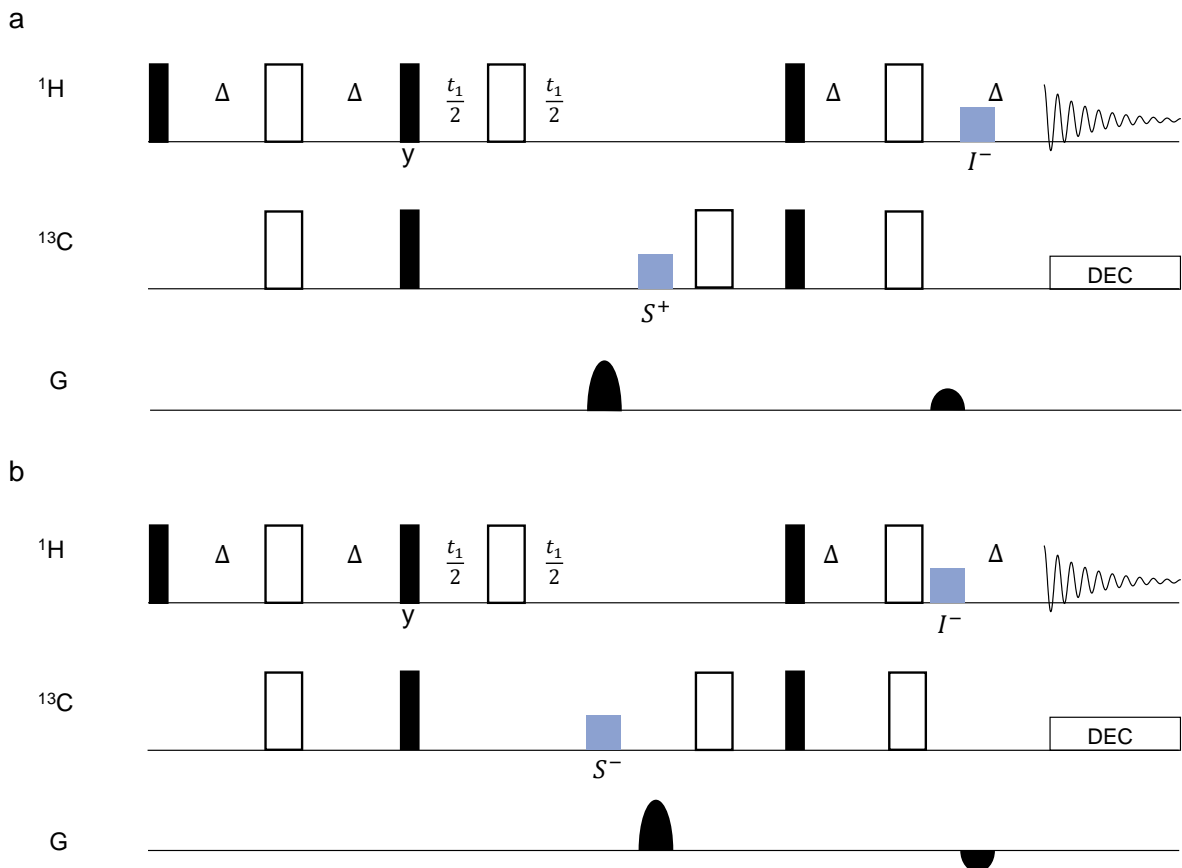
Figure 4. The scheme for gradient pulse compensation in a parallel HSQC pulse sequence involves blocks (colored in blue) indicating the CLOC pulse. The gradient pulse ratio in detector 1 (a) was set to 4:1 to select the $S^+ \to I^-$ pathway. In detector 2 (b), the gradient pulse ratio was set to 4:-1 to select the $S^- \to I^-$ pathway. The black blocks represent $\pi/2$ pulses and the white blocks represent π pulses, with all phases set to 0 unless specifically noted. $\Delta = 1/4J$. The protected coherences are labeled below the CLOC blocks.

A pulse sequence tailored for parallel HSQC is illustrated in Fig. 4, in which the fundamental HSQC sequences were implemented in detectors 1 and 2. The gradient ratio in detector 1 was set to $4:1$ to select the $S^+ \to I^-$ pathway (Fig. 4a), while in detector 2, it was adjusted to $4:-1$ to select the $S^- \to I^-$ pathway (Fig. 4b). The compensation CLOC pulses, indicated in blue, were applied in detector 1 while the gradient pulses were applied in detector 2, and vice versa. The gradient pulses in parallel detectors were executed with a slight time delay to allow the insertion of the CLOC pulses. Each compensation pulse was applied to lock onto the relevant coherence. For instance, the first CLOC block in detector

1 was applied on ^{13}C to protect S^+ and its J coupling-induced product $I_z S^+$. The protected coherences are labeled below the CLOC pulses in Fig. 4. With this approach, the CLOC pulse must be designed to compensate for gradient spillover (effectively a range of frequency offsets) to protect one or more desired coherences.

115   In the pulse optimization, both the source and target states were specified as the locked coherence. When a gradient pulse is applied, its shape and duration remain fixed, while its amplitude can vary. The optimization of CLOC pulses adheres to this principle. Specifically, the gradient pulse contributes to a time-dependent drift Hamiltonian $\mathbf{H}_g(t) = A\sin(\pi t/\tau)\mathbf{H}_{z0}$, where $\mathbf{H}_{z0}$ represents the Zeeman Hamiltonian under a 1 T field, $\tau = 1$ ms is the gradient pulse duration. To cover a maximum B_0 drift of ± 0.06 Gauss measured with the parallel probe, the maximum B_0 drift of ± 0.25 Gauss was specified

120 for the CLOC pulse. Therefore, multiple time-dependent drifts were included in the optimization to account for both spatial and temporal variations in B_0 drifts. The RF amplitude in the ^{1}H channel was set to 6 kHz with a $\pm 20\%$ B_1 inhomogeneity, covering a 7 kHz bandwidth and simultaneously a maximum B_0 drift of ± 0.25 Gauss, corresponding to ± 1.07 kHz offset. For the ^{13}C channel, the RF amplitude was adjusted to 4 kHz with a $\pm 15\%$ B_1 inhomogeneity, covering a 6 kHz bandwidth and simultaneously a maximum B_0 drift of ± 0.25 Gauss. Decoupling of heteronuclear J-coupling is

125 demonstrated below, and the compensation for homonuclear J-coupling is discussed in Supplementary Note 4. Although concurrent optimization can explicitly include the J-coupling term in the system Hamiltonian, it involves parameters from two spins, resulting in a large model. Therefore, the strategy is to build optimal control for a single spin and test its heteronuclear decoupling effect within the designed bandwidth. The decoupling effect was quantified using average Hamiltonian theory (Waugh, 1982). The J-coupling scale factor is given by:

130 $$\chi = \mathrm{norm}(\bar{\mathbf{c}}) \tag{3}$$

where $\mathbf{c}$ is the time-dependent J-coupling tensor in the toggling frame, defined by the RF pulse plus resonance offset (see Supplementary Note 4). Fig. 5 displays the χ values for CLOC pulses designed for universal locking of I^+, I^-, and I_z of a single spin. A single CLOC pulse reduces heteronuclear J-coupling by less than 10% across the designed resonance offset and B_1 inhomogeneity range, see Fig. 5a and Fig. 5b. Given a pulse duration of 1 ms, heteronuclear J-couplings

135 smaller than or on the order of hundreds of Hz can be ignored as $\chi J \tau \ll 1$. This treatment also applies to coupling with a third spin when studying ^{1}H and ^{13}C, such as J_{CN} and J_{HN} in proteins (LeMaster and Richards, 1985; Liu and Prestegard, 2009). Fig. 5c shows residual coupling exists when two CLOC pulses are applied simultaneously to ^{1}H and ^{13}C. However, it does not imply the decoupling fails as χ sums all the items of the heteronuclear J-coupling tensor. One can also calculate the coherence-locking efficiency when double-quantum coherences require protection. The coherence-locking for

140 double-quantum coherence was tested by simulating an HMQC sequence, as detailed in Supplementary Note 7.
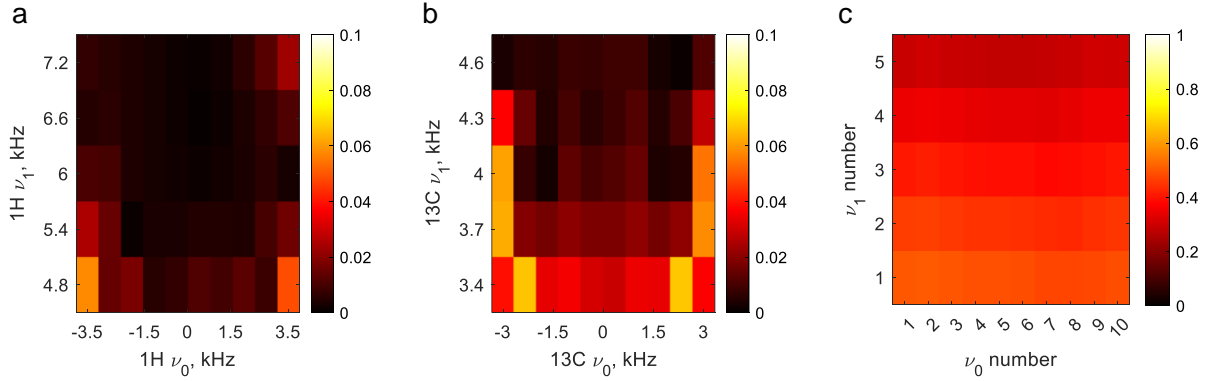
Figure 5. Scale factor χ of the J_{HC} coupling as a function of resonance offset and B_1 amplitude. (a) The CLOC pulse is applied to ^{1}H while ^{13}C is on resonance. (b) The CLOC pulse is applied to ^{13}C while ^{1}H is on resonance. (c) The CLOC pulses are applied simultaneously to ^{1}H and ^{13}C, with ν_0 on both channels aligned, and ν_1 on both channels aligned.

Using this strategy, the simulated locking efficiency of the optimal control pulses is depicted in Fig. 6. The sample was segmented into 12 voxels along the z-direction, and the spin trajectory for each voxel was computed while simultaneously executing a CLOC pulse and a coupled gradient pulse, which induced a maximum B_0 drift of ±0.25 Gauss. Fig. 6a illustrates that the ensemble spin states start from I^- and oscillate between -1 and 1 while remaining confined within a narrow range, and go back to I^- at the end of 1 ms gradient pulse. Fig. 6b and Fig. 6c show the evolution of ensemble spin states starting from S^+ and I^-S^+, respectively. Additionally, Fig. 6d-f present the spin trajectory with the same initial states but without coherence locking for comparison, indicating coherence dephasing caused by the coupled gradient.
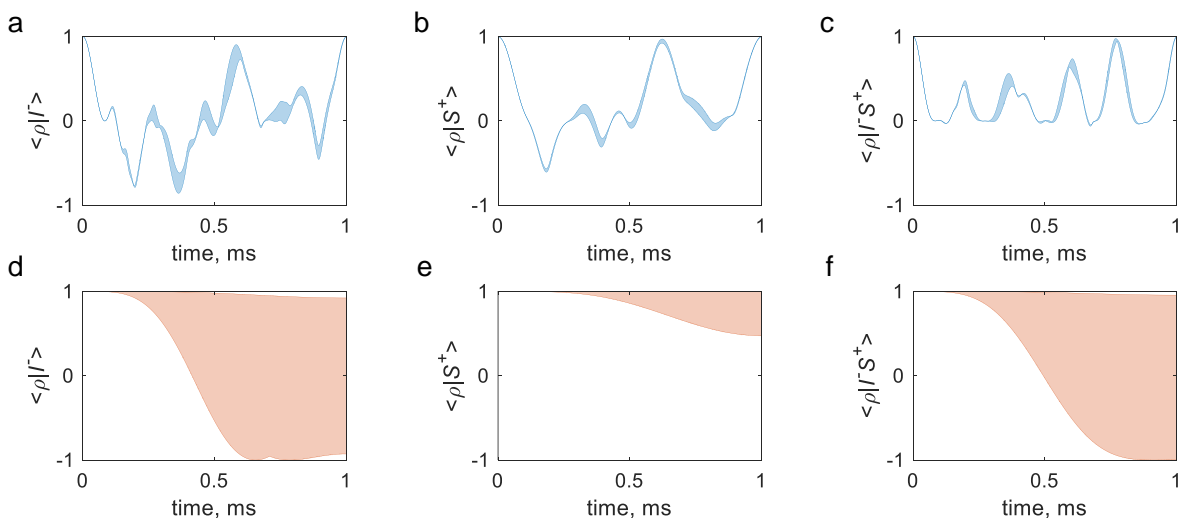
Figure 6. Ensemble spin trajectory subject to the gradient field spillover dephasing. (a,b,c) represent the trajectories starting from I^-, S^+ and I^-S^+ with the CLOC pulses applied to ^{1}H, ^{13}C and ^{1}H & ^{13}C, respectively. (d,e,f) correspond to the respective trajectories without CLOC pulses. The real values of the inner product are displayed. The ^{1}H and ^{13}C were on resonance, and the J coupling constant was 145 Hz. The RF amplitudes were 6 kHz for ^{1}H and 4 kHz for ^{13}C.

The parallel HSQC pulse sequence was tested using a parallel probe (see Methods for details), two detectors of the probe were used, with 0.6 M glycine-2-^{13}C in D$_2$O in detector 1 and 0.3 M D-glucose-^{13}C$_6$ in D$_2$O in detector 2. The resulting spectra are presented in Fig. 7, where the 1D projections of the ^{1}H and ^{13}C signals from the 2D spectrum are displayed to illustrate the signal intensity for three cases. The single-detector scenario (grey) serves as a reference, while the orange lines represent amplitude-suppressed signals caused by gradient spillover-induced dephasing. In contrast, the blue lines correspond to the results of parallel operation with coherence-locking, demonstrating signal intensity recovery and effective dephasing compensation. Suppose the CLOC pulses effectively achieve broadband locking for both the ^{1}H and ^{13}C spin coherences, such that each peak in the coherence-locking case has the same intensity as in the reference case. However, in Fig. 7b, slight intensity differences are observed between the coherence-locking results and the reference, particularly for the peaks at 3.8 ppm and 3.9 ppm in the ^{1}H dimension, correlating to 72.8 ppm and 79.1 ppm in the ^{13}C dimension, respectively. Since the pulse optimization did not compensate for homonuclear coupling (^{1}H-^{1}H and ^{13}C-^{13}C), coherence-locking efficiency is degraded, especially when the offset difference between two peaks is comparable to the homonuclear J-coupling constant. A comparison of D-glucose-^{13}C$_6$ HSQC spectra with and without homonuclear coupling

is provided in Fig. S8. The discrepancies also arise from the chemical shift dependence of coherence-locking efficiency. For instance, each CLOC pulse introduces slight phase distortion; if each pulse has a fidelity of 95%, the combined fidelity of two pulses reduces to 90%. The robustness of CLOC pulses encompasses factors including bandwidth, B_1 inhomogeneity, and gradient amplitude, which are detailed in Supplementary Note 5. In addition, coherence-locking can also be influenced by RF coupling, when a CLOC pulse is applied in detector 1, weak RF signals (about 1% at 500 MHz (He et al., 2024)) may transfer from detector 1 to detector 2, distorting the spin state. Hence, the CLOC pulse was adjusted to relatively lower amplitudes, i.e., 6 kHz for ^{1}H and 4 kHz for ^{13}C. The corresponding power levels were 0.43 W for the ^{1}H channel, and 2.3 W for the ^{13}C channel on detector 2, making the RF coupling effect more significant in the ^{13}C channel, highlighting the challenges of coherence locking for low-sensitive nuclei when a large bandwidth is required.
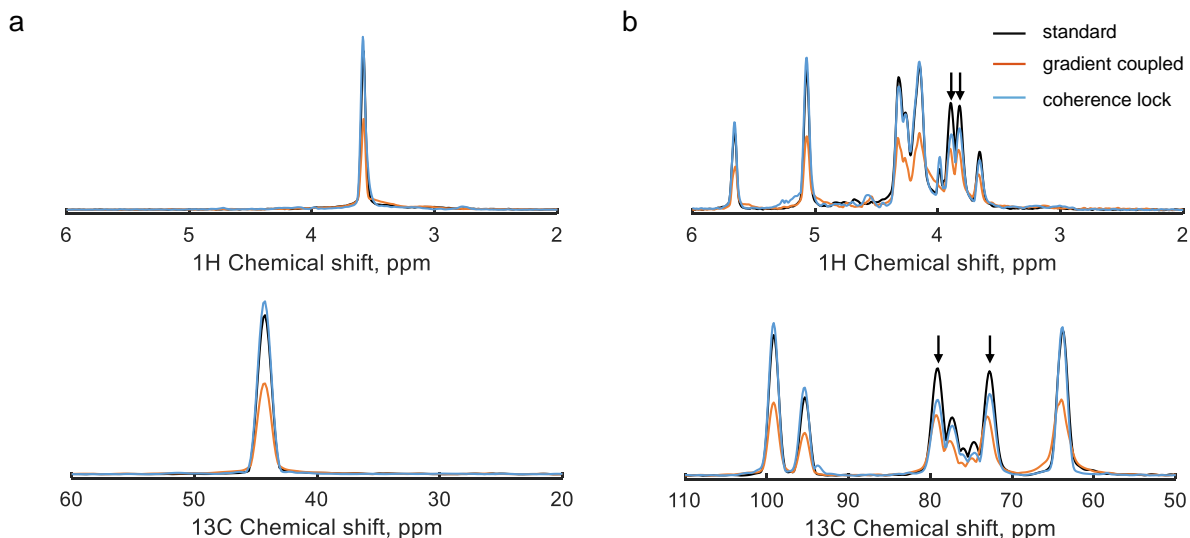
Figure 7. Experimental parallel HSQC spectra of glycine-2-^{13}C (a) and D-glucose-^{13}C$_6$ (b) respectively, using the pulse sequence in Fig. 4. The grey lines represent the results without gradient coupling, as a reference. The orange lines display the spectrum under gradient spillover (no compensation), and the blue lines display the results with coherence-locking compensation.

3 Conclusion

We employed CLOC pulses to protect specific coherences from gradient spillover in a parallel NMR setup. This approach effectively compensates for gradient-induced phase shifts, preserving coherence and signal integrity across

parallel detectors, as demonstrated in a parallel HSQC experiment. This optimal control-assisted coherence locking provides an alternative strategy for designing coherence protection protocols.

175 Although we tested the heteronuclear decoupling effect of specific optimal pulses, general optimal pulses could potentially average out the heteronuclear coupling due to their "noise-like" waveforms. The overall strategy is to establish the locking of a single spin and validate its decoupling, thereby avoiding the complexity of a coupled spin model. While the CLOC pulses protect the targeted coherences, allowing coherence evolution to be neglected during this period, it should be excluded when calculating the J-coupling evolution delay.

180 The limitations of this approach can stem from RF coupling between multiple detectors and homonuclear coupling in a general spin system. As shown by a parallel HSQC experiment and HMQC simulations, single-spin coherence can be universally locked in a general spin system, while double-quantum coherences (IS) can be locked using two simultaneous locking pulses. However, locking higher-order heteronuclear coherence is challenging in practice, as multiple coherence-locking pulses can introduce significant RF coupling. Although optimal control can compensate for

185 homonuclear coupling at the cost of increased RF power, the compensation fails when two spins have a small chemical shift difference and exhibit second-order spectra, where the RF Hamiltonian commutes with the J-coupling term, and the Zeeman term nearly commutes with the J-coupling term. Both high-order coherence locking and homonuclear decoupling require additional RF power, a broader approach may jointly compensate for RF coupling and gradient spillover effects. The limitation of extending this scheme to higher parallelism also arises from relaxation decay, which increases with more

190 alternating gradient pulses.

This work discussed conducting the same pulse sequence in two detectors with different gradient ratios. When the detectors perform different experiments, such as HMQC on detector 1 and HSQC on detector 2, the relaxation delay on each detector can be adjusted to synchronize the parallel pulses. However, because the acquisition is no longer simultaneous, addressing the RF coupling between the pulse and FID in the acquisition stage is beyond the scope of

195 this work.

4 Methods

For sample preparation, a 10% H_2O/90% D_2O solution was prepared to measure the gradient strength and gradient spillover ratio. Two solutions were prepared in D_2O (99.9%): a 0.6 M glycine-2-^{13}C solution and a 0.3 M D-glucose-[13]C_6 solution for the parallel HSQC experiment. The same glycine-2-^{13}C solution was also used for the PGSE experiment. The

samples were loaded into syringes and manually pumped into the individual fluidic chambers of the dedicated detector. The D_2O, glycine-2-^{13}C and D-glucose-$^{13}C_6$ were purchased from Sigma-Aldrich.

Experimental validation was performed using a 4-detector parallel NMR probe (Voxalytic GmbH), as shown in Fig. S12, which was installed in a Bruker AVANCE NEO 11.7 T (^{1}H frequency 500.13 MHz) NMR system (Bruker BioSpin GmbH). For demonstration, 2 of the 4 detectors were used, each double-resonant (^{1}H/^{13}C) and equipped with an independent single-axis pulsed field gradient. The two gradient channels were powered by the Bruker GREAT micro-imaging amplifiers using a customized cable splitting the three amplifiers from a single cable to three individual cables (Bruker). Pulse calibration was conducted for each detector individually. In detector 1, a hard 90° ^{1}H of pulse length 7.4 μs was applied at 20 W, a hard 90° ^{13}C pulse of length 25 μs was applied at 25 W, with a corresponding value in detector 2 of 6.1 μs for ^{1}H and 19.0 μs for ^{13}C. The power levels were then scaled down for the CLOC pulses with low amplitudes. The HSQC contained 256 t_1 increments, each with 1 scan of 1024 data points. A total of 32 dummy scans were executed to stabilize the spin system before data collection, the relaxation delay is 1 second and the receiver gain is 10. The sweep width was 10 ppm for ^{1}H and 150 ppm for ^{13}C. Experiments explicitly run in parallel were done using the multireceive option in TopSpin 4.1.3. The parallel HSQC experiments were repeated twice for good shimming quality: data from detector 1 was collected with global shimming focused on detector 1, and data from detector 2 was collected with shimming focused on detector 2.

The magnetic field simulation was conducted with the finite element method software COMSOL MultiPhysics 6.1 (COMSOL AB, Sweden), and the simulated data was processed with Matlab 2023b (MathWorks Inc., USA). The pulse optimization and spin dynamics calculations were completed with Spinach v2.8 (Hogben et al., 2011), the detailed setting for optimal control is provided in Supplementary Note 3.

Acknowledgements

M.H. is supported by the Joint Lab Virtual Materials Design (JLVMD) of the Helmholtz Association, Germany. J.G.K. acknowledges support from the ERC-SyG (HiSCORE, 951459). N.M., B.L., and J.G.K. acknowledge partial support from CRC 1527 HyPERiON. The authors acknowledge the support of the Helmholtz Society through the program Materials Systems Engineering. M.H. acknowledges support from the state of Baden-Württemberg through the bwHPC BwUniCluster 2.0. We acknowledge Dr. Thomas Oerther (Bruker BioSpin GmbH Co. KG) for support in running the GREAT imaging gradient amplifiers for parallel NMR spectroscopy experiments. We appreciate Prof. Ilya Kuprov's suggestions on Spinach simulations.

Code and data availability

The Matlab code and experimental data are available at https://doi.org/10.5281/zenodo.15188023(He et al., 2025).

Author contributions

230   J.G.K. and N.M. conceived the pulse compensation idea. M.H. performed the simulations with input from all coauthors. M.H. and N.M. drafted the manuscript. M.H., N.M. and D.B. conducted the experiments. All authors reviewed and refined the manuscript. J.G.K., B.L. and N.M. provided supervision and secured the funding.

Competing interests

235   J.G.K. serves on the editorial board of *Magnetic Resonance* and is a shareholder of Voxalytic GmbH, a spinoff company that produces and markets microscale NMR devices. The other authors declare no competing interests.

References

Barskiy, D. A., Salnikov, O. G., Romanov, A. S., Feldman, M. A., Coffey, A. M., Kovtunov, K. V., Koptyug, I. V., and Chekmenev, E. Y.: NMR Spin-Lock Induced Crossing (SLIC) Dispersion and Long-Lived Spin States of Gaseous Propane at Low Magnetic Field (0.05T), J. Magn. Reson., 276, 78–85, https://doi.org/10.1016/j.jmr.2017.01.014, 2017.

Becker, M., Cheng, Y.-T., Voigt, A., Chenakkara, A., He, M., Lehmkuhl, S., Jouda, M., and Korvink, J. G.: Artificial Intelligence-Driven Shimming for Parallel High Field Nuclear Magnetic Resonance, Sci. Rep., 13, 17 983, https://doi.org/10.1038/s41598-023-45021-6, 2023.

Cheng, Y.-T., Jouda, M., and Korvink, J.: Sample-Centred Shimming Enables Independent Parallel NMR Detection, Sci. Rep., 12, 14 149, https://doi.org/10.1038/s41598-022-17694-y, 2022.

Ciobanu, L., Jayawickrama, D. A., Zhang, X., Webb, A. G., and Sweedler, J. V.: Measuring Reaction Kinetics by Using Multiple Microcoil NMR Spectroscopy, Angew. Chem. Int. Ed., 42, 4669–4672, https://doi.org/10.1002/anie.200351901, 2003.

DeVience, S. J., Walsworth, R. L., and Rosen, M. S.: Nuclear Spin Singlet States as a Contrast Mechanism for NMR Spectroscopy, NMR Biomed., 26, 1204–1212, https://doi.org/10.1002/nbm.2936, 2013a.

DeVience, S. J., Walsworth, R. L., and Rosen, M. S.: Preparation of Nuclear Spin Singlet States Using Spin-Lock Induced Crossing, Phys. Rev. Lett., 111, 173 002, https://doi.org/10.1103/PhysRevLett.111.173002, 2013b.

DeVience, S. J., Walsworth, R. L., and Rosen, M. S.: Probing Scalar Coupling Differences via Long-Lived Singlet States, J. Magn. Reson., 262, 5761, https://doi.org/10.1016/j.jmr.2015.12.003, 2015.

DeVience, S. J., Greer, M., Mandal, S., and Rosen, M. S.: Homonuclear J-Coupling Spectroscopy at Low Magnetic Fields Using Spin-Lock Induced Crossing**, ChemPhysChem, 22, 2128–2137, https://doi.org/10.1002/cphc.202100162, 2021.

Gram, M., Seethaler, M., Gensler, D., Oberberger, J., Jakob, P. M., and Nordbeck, P.: Balanced Spin-Lock Preparation for B_1-Insensitive and B_0-Insensitive Quantification of the Rotating Frame Relaxation Time $T_{1\rho}$, Magn. Reson. Med., 85, 2771–2780, https://doi.org/10.1002/mrm.28585, 2021.

Grzesiek, S. and Bax, A.: Spin-Locked Multiple Quantum Coherence for Signal Enhancement in Heteronuclear Multidimensional NMR Experiments, J. Biomol. NMR, 6, 335–339, https://doi.org/10.1007/BF00197815, 1995.

He, M., Faderl, D., MacKinnon, N., Cheng, Y.-T., Buyens, D., Jouda, M., Luy, B., and Korvink, J. G.: A Digital Twin for Parallel Liquid-State Nuclear Magnetic Resonance Spectroscopy, Commun. Eng., 3, 1–13, https://doi.org/10.1038/s44172-024-00233-0, 2024.

He, M., MacKinnon, N., Buyens, D., Luy, B., and Korvink, J. G.: Coherence locking in a parallel NMR probe defends against gradient field spillover, Zenodo [data set], https://doi.org/10.5281/zenodo.15188023, 2025.

Hogben, H. J., Krzystyniak, M., Charnock, G. T., Hore, P. J., and Kuprov, I.: Spinach–a Software Library for Simulation of Spin Dynamics in Large Spin Systems, J. Magn. Reson., 208, 179–194, https://doi.org/10.1016/j.jmr.2010.11.008, 2011.

Holz, M. and Weingartner, H.: Calibration in Accurate Spin-Echo Self-Diffusion Measurements Using 1H and Less-Common Nuclei, J. Magn. Res. (1969), 92, 115–125, https://doi.org/10.1016/0022-2364(91)90252-O, 1991.

270   Hou, T., MacNamara, E., and Raftery, D.: NMR Analysis of Multiple Samples Using Parallel Coils: Improved Performance Using Reference Deconvolution and Multidimensional Methods, Anal. Chim. Acta, 400, 297–305, https://doi.org/10.1016/S0003-2670(99)00706-0, 1999.

Jiang, B. and Chen, W.: On-Resonance and off-Resonance Continuous Wave Constant Amplitude Spin-Lock and $T_{1\rho}$ Quantification in the Presence of B_1 and B_0 Inhomogeneities, NMR Biomed., 31, e3928, https://doi.org/10.1002/nbm.3928, 2018.

275   Kim, Y., Liu, M., and Hilty, C.: Parallelized Ligand Screening Using Dissolution Dynamic Nuclear Polarization, Anal. Chem., 88, 11 178–11 183, https://doi.org/10.1021/acs.analchem.6b03382, 2016.

Kovtunov, K. V., Truong, M. L., Barskiy, D. A., Koptyug, I. V., Coffey, A. M., Waddell, K. W., and Chekmenev, E. Y.: Long-Lived Spin States for Low-Field Hyperpolarized Gas MRI, Chem. – Eur. J., 20, 14 629–14 632, https://doi.org/10.1002/chem.201405063, 2014.

Kupče, Ē., Frydman, L., Webb, A. G., Yong, J. R. J., and Claridge, T. D. W.: Parallel Nuclear Magnetic Resonance Spectroscopy, Nat.
280   Rev. Methods Primers, 1, 1–23, https://doi.org/10.1038/s43586-021-00024-3, 2021.

Lei, K.-M., Ha, D., Song, Y.-Q., Westervelt, R. M., Martins, R., Mak, P.-I., and Ham, D.: Portable NMR with Parallelism, Anal. Chem., 92, 2112–2120, https://doi.org/10.1021/acs.analchem.9b04633, 2020.

LeMaster, D. M. and Richards, F. M.: Proton-nitrogen-15 heteronuclear NMR studies of Escherichia coli thioredoxin in samples isotopically labeled by residue type, Biochemistry, 24, 7263–7268, 1985.

285   Li, Y., Wolters, A. M., Malawey, P. V., Sweedler, J. V., and Webb, A. G.: Multiple Solenoidal Microcoil Probes for High-Sensitivity, High-Throughput Nuclear Magnetic Resonance Spectroscopy, Anal. Chem., 71, 4815–4820, https://doi.org/10.1021/ac990855y, 1999.

Liu, Y. and Prestegard, J. H.: Measurement of one and two bond N–C couplings in large proteins by TROSY-based J-modulation experiments, J. Magn. Reson., 200, 109–118, 2009.

290   MacNamara, E., Hou, T., Fisher, G., Williams, S., and Raftery, D.: Multiplex Sample NMR: An Approach to High-Throughput NMR Using a Parallel Coil Probe, Anal. Chim. Acta, 397, 9–16, https://doi.org/10.1016/S0003-2670(99)00387-6, 1999.

Rodin, B. A., Kiryutin, A. S., Yurkovskaya, A. V., Ivanov, K. L., Yamamoto, S., Sato, K., and Takui, T.: Using Optimal Control Methods with Constraints to Generate Singlet States in NMR, J. Magn. Reson., 291, 14–22, https://doi.org/10.1016/j.jmr.2018.03.005, 2018.

Ross, A., Schlotterbeck, G., Senn, H., and von Kienlin, M.: Application of Chemical Shift Imaging for
295   Simultaneous and Fast Acquisition of NMR Spectra on Multiple Samples, Angew. Chem. Int. Ed., 40, 3243–3245, https://doi.org/10.1002/1521-3773(20010903)40:17<3243::AID-ANIE3243>3.0.CO;2-F, 2001.

Sonnefeld, A., Razanahoera, A., Pelupessy, P., Bodenhausen, G., and Sheberstov, K.: Long-Lived States of Methylene Protons in Achiral Molecules, Sci. Adv., 8, eade2113, https://doi.org/10.1126/sciadv.ade2113, 2022.

Stejskal, E. O. and Tanner, J. E.: Spin Diffusion Measurements: Spin Echoes in the Presence of a Time-Dependent Field Gradient, J.
Chem. Phys., 42, 288–292, https://doi.org/10.1063/1.1695690, 1965.

Wang, H., Ciobanu, L., Edison, A. S., and Webb, A. G.: An Eight-Coil High-Frequency Probehead Design for High-Throughput Nuclear
Magnetic Resonance Spectroscopy, J. Magn. Reson., 170, 206–12, https://doi.org/10.1016/j.jmr.2004.07.001, 2004.

Waugh, J. S.: Theory of Broadband Spin Decoupling, J. Magn. Reson., 50, 30–49, https://doi.org/10.1016/0022-2364(82)90029-4, 1982.

300